


# Anomalous valley Hall effect induced by mirror symmetry breaking in transition metal dichalcogenides

Shilei Ji , Ruijia Yao, and Chuye Quan*Institute of Advanced Materials (IAM), Nanjing University of Posts and Telecommunications (NJUPT), Nanjing 210023, China*

Jianping Yang

*School of Science, Nanjing University of Posts and Telecommunications (NJUPT), Nanjing 210023, China*

Fabio Caruso\*

*Institut für Theoretische Physik und Astrophysik, Christian-Albrechts-Universität zu Kiel, Kiel 24118, Germany  
and Kiel Nano, Surface and Interface Science KiNSIS, Kiel 24118, Germany*Xing'ao Li *School of Science, Nanjing University of Posts and Telecommunications (NJUPT), Nanjing 210023, China  
and College of Science, Zhejiang University of Science and Technology, Hangzhou 310023, China*

(Received 18 March 2023; revised 7 May 2023; accepted 9 May 2023; published 31 May 2023)

The control of the valley degree of freedom in Bloch electrons has opened up new avenues for information processing. The synthesis of ferrovalley materials, however, has been limited due to the stringent requirements for breaking both time and space inversion symmetries. To address this challenge, we propose a Janus method for inducing valley polarization in nonmagnetic transition metal dichalcogenides. Our study shows that the magnetic moment in monolayer TiTeI arises from the breaking of mirror symmetry and the presence of unpaired electrons. The Stoner criterion  $I_{ex}N(E_F) > 1$  confirms that the band splitting originates from the  $d$  orbital of titanium. Moreover, the exchange interaction combined with spin-orbit coupling opens up the valley splitting. The anomalous valley Hall effect (AVHE) can be realized by applying an in-plane electric field, as a result of the valley-contrasting Berry curvature. The modulation of valley-selective circular dichroism and AVHE by optical, electronic, and magnetic fields make TiTeI a promising material for future studies and applications in valleytronics.

DOI: [10.1103/PhysRevB.107.174434](https://doi.org/10.1103/PhysRevB.107.174434)

## I. INTRODUCTION

Valleytronics is a relatively new area that focuses on the manipulation of electronic valleys in a ferrovalley material, rather than the manipulation of electron spins, which is the foundation of spintronics [1–6]. One of the key features of valleytronics is the fact that valleys have a unique and well-defined momentum, which can be used to encode information. Unlike an electron spin, which can be easily disturbed by quasiparticle interactions, magnetic impurities, or thermal fluctuations, valleys are more robust and can be used to store and process information.

In recent years, there has been a shift towards the study of valleys in two-dimensional materials, such as transition metal dichalcogenides (TMDs) [5,7–10]. This is due to the unique electronic and optical properties of TMDs, which makes them suitable for valleytronic applications. TMDs, as a result of broken inversion symmetry, possess two inequivalent valleys at the  $K$  point in momentum space, which are referred to as

the valley degree of freedom [10–12]. Tight-binding models combined with *ab initio* calculations demonstrate the coupling of spin and valley in MoS<sub>2</sub>, highlighting the importance of space inversion symmetry breaking and spin-orbit coupling [10]. It has also been found that both the valley Hall effect and spin Hall effect can exist simultaneously in carrier-doped MoS<sub>2</sub> [11]. Valley polarization can be achieved via the optical absorption of circularly polarized photons or breaking the valley degeneracy of the system, which is protected by time-reversal symmetry [2,11,13,14].

Based on these methods, Tong *et al.* breaks the degeneracy valley by inducing intrinsic ferromagnetism in TMDs by *ab initio* calculations [5]. The exchange interaction of transition metal  $d$  electrons, induced by time-reversal symmetry breaking, lifts the valley degeneracy, leading to a splitting of the carrier energies in the valence and conduction bands at the  $K$  and  $K'$  high-symmetry points. Moreover, the recent synthesis of Janus MoSSe [15], where a layer of S atoms is replaced by Se, demonstrates the retention of the excellent performance of MoS<sub>2</sub> while also introducing a vertical dipole moment and enhanced Rashba spin-orbit coupling [16]. As a result, the exploration of intrinsic valley polarization in Janus  $MXY$  (such as LaBrI, VSSe, and VClBr) has gained traction [17–20].

\*caruso@physik.uni-kiel.de

†lxahbmy@126.com

However, the ferromagnetic properties of  $MXY$ , as described above, are constrained by the ferromagnetic behavior of  $MX_2$ . In the event of  $MX_2$  exhibiting nonmagnetic characteristics,  $MXY$  would not be able to maintain long-range magnetic order. Furthermore, the synthesis of many  $MX_2$  has yet to be achieved experimentally, limiting the application and exploration of Janus materials. Hence, the question remains: Can intrinsic ferromagnetism be induced in nonmagnetic TMD materials through the Janus method?

In this study, we have successfully closed this gap by inducing ferromagnetism in the nonmagnetic material  $\text{TiI}_2$ . The breaking of the mirror symmetry in  $\text{TiTeI}$  results in a reduction of symmetry to  $C_{3v}$ . Our analysis of the density of states and the Stoner criterion shows that  $\text{TiTeI}$  has an intrinsic ferromagnetism, which is attributed to the Ti atom. Additionally, compared to  $\text{TiI}_2$ , a valley splitting up to 83 meV occurs in  $\text{TiTeI}$ . Our investigation based on the tight-binding model with an *ab initio* calculation reveals that the valley splitting arises from the exchange interaction and the spin-orbit coupling. By incorporating a many-body formalism based on the Bethe-Salpeter equation (BSE), our calculations demonstrate that  $\text{TiTeI}$  exhibits valley-selective circular dichroism, leading to the emergence of excitonic states characterized by a well-defined valley index. Furthermore, our results suggest the presence of a fascinating anomalous valley Hall effect (AVHE) in  $\text{TiTeI}$ , indicated by Berry curvatures with opposite signs. Regardless of the orientation of the magnetic moment, the Berry curvature at the valley is always locked.

## II. METHODS

First-principles calculations are performed within the frame of density functional theory (DFT) using the Vienna Ab initio simulation package (VASP) based on the projected augmented wave (PAW) method [21–23]. The electron configurations of the Ti, Te, and I atom are  $3p^6 4s^2 3d^2$ ,  $5s^2 5p^4$ , and  $5s^2 5p^5$ , respectively. The plane-wave cutoff energy is set to 500 eV and a  $k$ -point grid of  $12 \times 12 \times 1$  is used. The force on each atom is smaller than  $1 \text{ meV } \text{\AA}^{-1}$ . A vacuum space of greater than  $15 \text{ \AA}$  is inserted along the  $z$  axis to avoid the interaction between adjacent layers. The weak van der Waals interaction considered in monolayer (1L)  $\text{TiTeI}$  is described by the DFT-D3 method [24]. The spin-orbit coupling (SOC) is considered in the band structure and magnetic anisotropy energy (MAE) calculations. The MAE calculation is defined as  $E_{100} - E_{001}$ , where a positive (negative) value indicates that the easy magnetization axis is interlayer (intralayer). The anomalous Hall conductivity based on Berry curvature is calculated on a denser  $k$  mesh of  $100 \times 100 \times 1$  for the 1L  $\text{TiTeI}$  by using the WANNI90 package [25–29].

*Ab initio* calculations of the optical absorption spectrum and the valley-selective circular dichroism are conducted with the full-potential all-electron code EXCITING [30–33]. A basis-set cutoff of  $|\mathbf{G} + \mathbf{K}|_{\text{max}}$  is set to 8.0, with a  $15 \times 15 \times 1$   $k$  grid. Additionally, the SOC effect and van der Waals interaction have been considered in all of the calculations. Local-field effects are included up to a cutoff of  $|\mathbf{G} + \mathbf{q}| = 3.0 \text{ Bohr}^{-1}$ . In addition, 100 unoccupied states were included in the calculation of the dielectric matrix for four valence and four conduction bands.

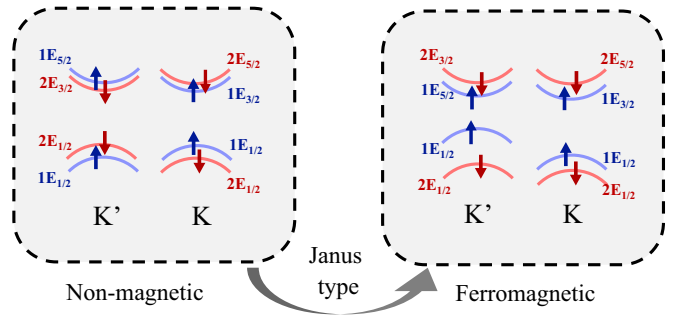


FIG. 1. The schematic valley at  $K$  and  $K'$ . Left and right panels represent the circularly polarized light absorption rules at a nonmagnetic and ferromagnetic system, respectively. Blue and red lines are the spin-up and spin-down channels.

## III. RESULTS AND DISCUSSION

### A. Two-band $\mathbf{k} \cdot \mathbf{p}$ model

Traditional TMD monolayers, such as  $\text{TiI}_2$ , possess a trigonal prismatic coordination ( $D_{3h}$ ) [9,34,35]. The conduction band (CB) maximum is primarily derived from the  $d_{z^2}$  orbital of the transition metal, while the top of the valence band (VB) is dominated by the hybridization between the  $d_{xy}$  and  $d_{x^2-y^2}$  orbitals. A two-band  $\mathbf{k} \cdot \mathbf{p}$  model can be used to describe the valley polarization at the  $K$  and  $K'$  points. The basic functions for the valence and conduction states in the  $D_{3h}$  group can be written as follows:

$$\psi_v^\tau = \frac{|d_{x^2-y^2}\rangle + i\tau|d_{xy}\rangle}{\sqrt{2}}, \quad (1a)$$

$$\psi_c^\tau = |d_{z^2}\rangle. \quad (1b)$$

The index  $\tau = +1$  ( $-1$ ) represents the  $K$  ( $K'$ ) valley, and  $v/c$  denotes the valence/conduction state. In order to verify the origin of valley polarization, we construct the two-band  $\mathbf{k} \cdot \mathbf{p}$  Hamiltonian with SOC around the  $K$  and  $K'$  valleys,

$$H_{\text{eff}} = \hat{s}_0 H_0 + H_{\text{soc}}, \quad (2a)$$

$$H_0 = \frac{\Delta}{2} \hat{\sigma}_z + v_F (\tau \hat{\sigma}_x k_x + \hat{\sigma}_y k_y), \quad (2b)$$

$$H_{\text{soc}} = \tau \hat{s}_z (\lambda_c \hat{\sigma}_+ + \lambda_v \hat{\sigma}_-), \quad (2c)$$

where  $v_F$  is the massless Fermi velocity of the Dirac electrons, and  $\hat{\sigma}_i$  and  $\hat{s}_i$  ( $i = 0, x, y, z$ ) are the Pauli matrices for pseudospin and spin, respectively.  $\lambda_v$  ( $\lambda_c$ ) is a SOC parameter for the valence (conduction) band.  $\hat{\sigma}_\pm$  is defined as  $\frac{1}{2}(\hat{\sigma}_0 \pm \hat{\sigma}_z)$ . Since valley polarization only occurs on the out-of-plane magnetic sequence, only the Zeeman-SOC is considered in the work. By diagonalizing the above effective Hamiltonian  $H_{\text{eff}}$ , we obtain the energy spectra,

$$E = \frac{1}{2} \left\{ \tau \hat{s}_z (\lambda_c + \lambda_v) \pm \sqrt{4v_F^2 (k_x^2 + k_y^2) + [\Delta + \tau \hat{s}_z (\lambda_c - \lambda_v)]^2} \right\}. \quad (3)$$

As is shown in the left panel of Fig. 1, the top of the VB at the  $K$  ( $K'$ ) valley is contributed by the spin-up (spin-down) channel. Thus, the band gap with SOC along the out-of-plane sequence is

$$E_g(K) = E_g(K') = \Delta + (\lambda_c - \lambda_v). \quad (4)$$

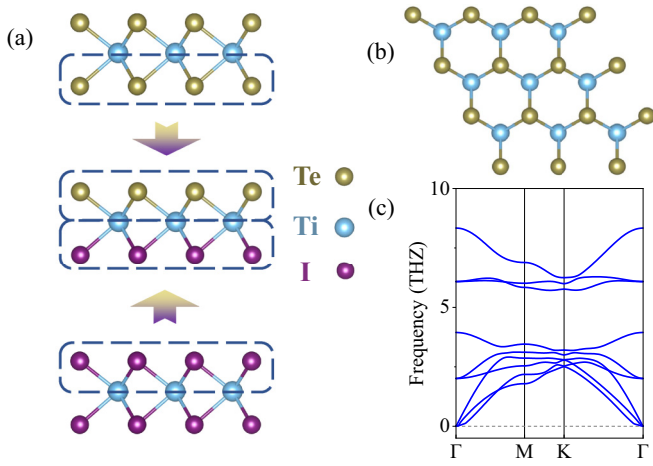


FIG. 2. The atomic structure of 1L TiTeI. (a) The side view and (b) the top view of the TMD. (c) The phonon dispersion along high-symmetry points.

For the nonmagnetic TMD, the SOC considering the pseudospin is still unable to induce valley splitting. Therefore, we introduce an exchange splitting term by considering a Janus TMD, which induces a nonzero net magnetic moment. The exchange splitting term can be written as

$$H_{\text{ex}} = -\hat{s}_z(m_c\hat{\sigma}_+ + m_v\hat{\sigma}_-), \quad (5)$$

where  $m_v$  ( $m_c$ ) denotes the effective exchange splitting of the valence (conduction) band. When considering the exchange splitting, the spin channels at the top of the VB for both  $K$  and  $K'$  valleys are spin up. The spin index is  $+1$ , and the Hamiltonian eigenvalues are expressed as

$$E = \frac{1}{2} \left\{ \tau(\lambda_c + \lambda_v) - (m_c + m_v) \pm \sqrt{4v_F^2(k_x^2 + k_y^2) + [\Delta + \tau(\lambda_c - \lambda_v) - (m_c - m_v)]^2} \right\}. \quad (6)$$

The band gap of the  $K$  and  $K'$  valleys is

$$E_g(K) = \Delta + (\lambda_c - \lambda_v) - (m_c - m_v), \quad (7a)$$

$$E_g(K') = \Delta - (\lambda_c - \lambda_v) - (m_c - m_v). \quad (7b)$$

Our analysis reveals that after considering the effect of SOC and exchange interaction, valley splitting emerged in TiTeI. The size of the valley splitting was found to be linearly correlated with the SOC strength of the Ti atom. The exchange interaction, in conjunction with the SOC effect, tends to couple the spin and valley, resulting in an intrinsic valley polarization.

### B. Mechanism of intrinsic ferromagnetism

In order to verify the accuracy of our  $\mathbf{k} \cdot \mathbf{p}$  model, we select  $\text{TiI}_2$  and  $\text{TiTeI}$  as the sample systems.  $\text{TiI}_2$ , as a traditional TMD, has been considered to be nonmagnetic when synthesized [35]. The crystal structures of 1L  $\text{TiI}_2$  and  $\text{TiTeI}$  are shown in Fig. 2(a). Unlike the traditional TMD, the Janus TMD breaks out-of-plane mirror symmetry and induces an out-of-plane dipole moment [36]. From the side view, the freestanding  $\text{TiTeI}$  is a sandwichlike structure composed of

Te(upper)-Ti(middle)-I(lower). The upper and lower layers can be considered as exfoliated from  $\text{TiTe}_2$  and  $\text{TiI}_2$ , respectively. The calculated lattice constant of  $\text{TiTeI}$  lies between those of  $\text{TiTe}_2$  and  $\text{TiI}_2$ , with the bond lengths of 2.80 Å and 2.91 Å for Ti-Te and Ti-I, respectively. This results in the reduction of the lattice symmetry from  $D_{3h}$  in  $\text{TiTe}_2$  and  $\text{TiI}_2$  to  $C_{3v}$  in  $\text{TiTeI}$ . The phonon dispersion along the high-symmetry points in the Brillouin zone has been plotted in Fig. 2(c), showing the absence of imaginary frequencies and indicating the dynamical stability of  $\text{TiTeI}$ .

In comparison to 1L  $\text{TiTe}_2$  and  $\text{TiI}_2$ , 1L  $\text{TiTeI}$  exhibits a net magnetic moment of  $1 \mu_B$ /unit cell. The chemical formula and oxidation state of  $\text{TiTeI}$  can be written as  $(\text{Te}^{2-})(\text{Ti}^{3+})(\text{I}^{1-})$ , with outermost electron orbitals of  $5p^4$ ,  $3d^2$ , and  $5p^5$ , respectively. It is found that the net magnetic moment in  $\text{TiTeI}$  originates from an unpaired electron in the compound. On the other hand, the chemical formula and oxidation state of  $\text{TiTe}_2$  and  $\text{TiI}_2$  are  $(\text{Te}^{2-})(\text{Ti}^{4+})(\text{Te}^{2-})$  and  $(\text{I}^{1-})(\text{Ti}^{2+})(\text{I}^{1-})$ , respectively. There are no unpaired electrons in either compound. In addition, the chemically similar 2D system  $\text{TiTe}_{2-x}\text{I}_x$  has been reported in the experiment [37]. A magnetoresistance response of  $\text{TiTe}_{2-x}\text{I}_x$  results from an unpaired electron on  $\text{Ti}^{3+}$ .

However, due to the different structure, the magnetic ground state of  $\text{TiTeI}$  in this work is not the same as  $\text{TiTe}_{2-x}\text{I}_x$ . For  $\text{TiTe}_{2-x}\text{I}_x$ , the structure is a 1T phase similar to  $\text{CrTe}_2$  and the magnetic ground state is antiferromagnetic, while the structure of  $\text{TiTeI}$  in this work is a 2H phase, which has a similar structure to  $\text{MoS}_2$ . To demonstrate the magnetic ground state, we calculate the Curie temperature of 2H- $\text{TiTeI}$ , which can determine how high the temperature can be for the ferromagnetic material to remain in ferromagnetism order. The anisotropic Heisenberg model with the nearest-neighbor exchange interaction has been applied to calculate the Curie temperature of the  $\text{TiTeI}$  monolayer in Fig. S2 in the Supplemental Material [38]. There is a peak at 265 K on the magnetic susceptibility, which shows that the Curie temperature of the  $\text{TiTeI}$  monolayer reaches 265 K. The high Curie temperature gives  $\text{TiTeI}$  a potential in valleytronic and spintronic applications. In addition, the net magnetic moment tends to  $1 \mu_B$ /unit cell at low temperatures, indicating that the magnetic ground state is ferromagnetic.

The Stoner criterion is a widely recognized method to determine the magnetic ground state at 0 K, which can be either ferromagnetic or paramagnetic. Starting from the spin-polarized and spin-unpolarized density of states (DOS) in Fig. S1 in the Supplemental Material [38], the Stoner criterion can be expressed mathematically as  $I_{\text{ex}}N(E_F)$ , where  $I_{\text{ex}}$  is the Stoner parameter and  $N(E_F)$  represents the spin-unpolarized DOS at the Fermi level.  $I_{\text{ex}}$  can be derived from the exchange splitting  $\Delta_{\text{ex}}$  as  $\Delta_{\text{ex}} = I_{\text{ex}}M$ . Here,  $\Delta_{\text{ex}}$  is the bands splitting between the opposite spin (more details can be obtained in Fig. S1 in the Supplemental Material [38]) and  $M$  is total magnetic moment per magnetic atom. The spin-unpolarized band structure shows that the half-filled band is contributed by Ti- $d$ . In contrast to Janus  $\text{LaBrI}$  [17], the large DOS in  $\text{TiTeI}$  mainly results from cationic electrons localized on Ti. Upon consideration of spin polarization, the half-filled band splits into spin-up and spin-down bands, leading to a large exchange splitting  $\Delta_{\text{ex}}$  of 1.16 eV in Fig. 3(b) and in Fig. S1

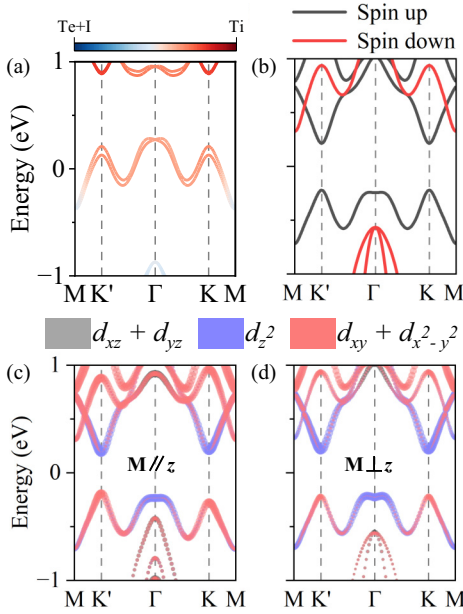


FIG. 3. The electronic structure of 1L TiTeI by DFT calculations. The band structure of 1L TiTeI (a) without spin polarization and with SOC, and (b) with spin polarization and without SOC. Dark and red lines represent spin-up and spin-down channels, respectively. The  $d$  orbital-resolved band structure with spin polarization and SOC for magnetic moment (c) parallel and (d) perpendicular to the  $z$  axis.

in the Supplemental Material [38]. This indicates that the net magnetic moment is contributed by Ti- $d$ . Therefore, in 1L TiTeI,  $I_{ex}N(E_F)$  equals 7.12, meeting the conditions for the establishment of ferromagnetism and the Stoner criterion  $I_{ex}N(E_F) > 1$  (Detailed parameters are given in Table I). As a result, 1L TiTeI exhibits intrinsic ferromagnetism, which originates from band splitting near the Fermi level induced by the Ti- $d$  orbital.

### C. Coupling between spin and valley

In Sec. III A, we have discussed valley polarization of TMDs based on the  $\mathbf{k} \cdot \mathbf{p}$  model. TiTeI, breaking spatial and time-reversal symmetry at the same time, has a robust valley splitting on an electronic structure. Subsequently, the band structure has been calculated using the PBE-SOC method [21]. The valley polarization originates from the exchange interaction and SOC effect. In Fig. 3(a), if only SOC is considered, there is a band splitting at valleys  $K$  and  $K'$ . The TiTeI monolayer is a metallic material with band splitting. If only the exchange interaction is considered in Fig. 3(b), the gap near the Fermi level is opened due to spin splitting. The TiTeI monolayer is a semiconductor material without valley

TABLE I. The parameters of the Stoner criterion, where the units of  $N(E_F)$ ,  $\Delta_{ex}$ ,  $M$ , and  $I_{ex}$  are states/eV, eV,  $\mu_B$ , and eV, respectively.

$N(E_F)$	$\Delta_{ex}$	$M$	$I_{ex}$	$I_{ex}N(E_F)$
6.14	1.16	1.00	1.16	7.12

splitting. When SOC and exchange interaction are considered at the same time in Fig. 3(c), the valley splitting can be revealed at the high-symmetry points  $K$  and  $K'$ , in agreement with the  $\mathbf{k} \cdot \mathbf{p}$  model depicted in Fig. 1. The valley splitting, represented as  $\Delta E_g = E_g(K) - E_g(K')$ , is found to be 83 meV in 1L TiTeI, which is a result of the breaking of mirror symmetry and the presence of the SOC effect. In contrast, the valley splitting in 1L TiI<sub>2</sub> was determined to be 0 meV due to time-reversal symmetry (Fig. S3 in the Supplemental Material [38]). The orbital-resolved band structure has been depicted in Fig. 3(c), where it is found that the spin-up Ti- $d_{z^2}$  orbitals occupy the bottom of the conduction band (CB), and the spin-up Ti- $d_{xy}$  and Ti- $d_{x^2-y^2}$  orbitals occupy the top of the valence band (VB). The in-plane magnetic moment is found to protect the degeneracy at  $K$  and  $K'$  in Fig. 3(d). In the subsequent analysis, the formula for coupling between the magnetization orientation and valley splitting is derived. The SOC Hamiltonian can be expressed as

$$\begin{aligned}
 H_{\text{soc}} &= \lambda \hat{L} \cdot \hat{S} \\
 &= \lambda (\hat{L}_x \cdot \hat{S}_x + \hat{L}_y \cdot \hat{S}_y + \hat{L}_z \cdot \hat{S}_z) \\
 &= \frac{\lambda}{2} (\hat{L}_+ \cdot \hat{S}_- + \hat{L}_- \cdot \hat{S}_+) + \lambda \hat{L}_z \cdot \hat{S}_z, \quad (8)
 \end{aligned}$$

where  $\lambda$  is the SOC strength and  $\hat{L}$  ( $\hat{S}$ ) is the orbital (spin) angular momentum. The raising and lowering operators are  $\hat{L}_{\pm} = \hat{L}_x \pm i\hat{L}_y$  and  $\hat{S}_{\pm} = \hat{S}_x \pm i\hat{S}_y$ . In addition, the bands at the VB and CB can be defined as  $E_v^{\tau} = \langle \psi_v^{\tau} | H_{\text{soc}} | \psi_v^{\tau} \rangle$  and  $E_c^{\tau} = \langle \psi_c^{\tau} | H_{\text{soc}} | \psi_c^{\tau} \rangle$ , respectively. Therefore, the gap between  $K$  and  $K'$  can be written as

$$\Delta E_v = i \langle d_{x^2-y^2} | H_{\text{soc}} | d_{xy} \rangle - i \langle d_{xy} | H_{\text{soc}} | d_{x^2-y^2} \rangle, \quad (9a)$$

$$\Delta E_c = i \langle d_{z^2} | H_{\text{soc}} | d_{z^2} \rangle - i \langle d_{z^2} | H_{\text{soc}} | d_{z^2} \rangle. \quad (9b)$$

In TiTeI, the CBM and VBM are both spin-up channels. For the parallel-spin state  $\langle d_{x^2-y^2} | H_{\text{soc}} | d_{xy} \rangle = -2|\lambda_v| i \cos \theta$ , the gap can be simplified as

$$\Delta E_v = 4|\lambda_v| \cos \theta, \quad (10a)$$

$$\Delta E_c = 0. \quad (10b)$$

Obviously, the SOC effect results in the nondegeneracy valley splitting at the VBM. When the magnetic moment switches to out-of-plane ( $\theta = 0$ ), the valley splitting reaches  $4|\lambda_v|$ , which is consistent with the above conclusion (Fig. S4 in the Supplemental Material [38]).

### D. Intrinsic valley-selective circular dichroism

Due to the interplay of  $C_3$  symmetry and the lack of an inversion center, we expect TiTeI to exhibit valley-selective circular dichroism, whereby the absorption of circularly polarized photons induces the formation of valley excitons at either the  $K$  or the  $K'$  valley, depending on the light helicity. In particular, left-handed photons can be absorbed to form an exciton at the  $K$  point in the Brillouin zone, while the formation of excitons at  $K'$  is symmetry forbidden. In contrast, right-handed photons can lead to the emergence of valley excitons at the  $K'$  high-symmetry points, leaving the  $K$  valley unaffected. Therefore, circularly polarized light is an effective method to excite and detect valley excitons. To investigate

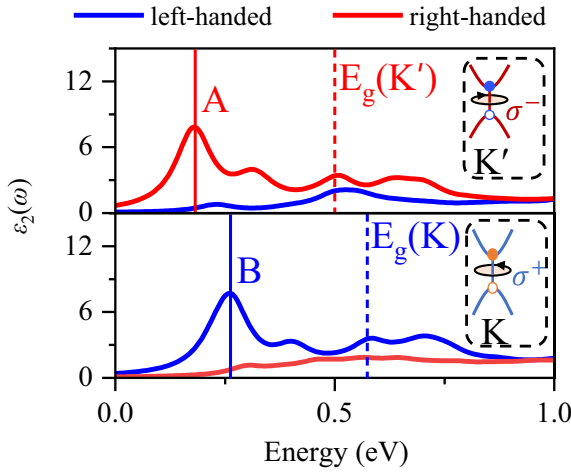


FIG. 4. The circular light absorption of 1L TiTeI. Upper panel: Circularly polarized light absorption at the  $K'$  valley. Lower panel: Circularly polarized light absorption at the  $K$  valley. Blue and red lines represent left- and right-handed polarization light, respectively. Moreover, red and blue vertical solid lines represent the location of excitons A and B. The band gap of the  $K'$  and  $K$  valleys has been marked as red and blue dashed lines.

valley-selective circular dichroism in TiTeI on a quantitative ground, we conduct *ab initio* calculations of the dielectric function based on the Bethe-Salpeter equation (BSE), and we explicitly take into account the circular polarization of light following the prescription of Ref. [39]. The macroscopic transverse dielectric tensor is  $\epsilon = \epsilon_1 + i\epsilon_2$ , where  $\epsilon_1$  and  $\epsilon_2$  are the real and imaginary parts of the macroscopic dielectric function, respectively. The imaginary part of the dielectric function in the vicinity of the  $K$  valley  $\epsilon_{2,K}$  can be defined by [39,40]

$$\epsilon_{2,K} = \frac{4\pi^2 e^2}{m_e^2 \Omega N_k} \sum_{\lambda} |\hat{\epsilon} \cdot \mathbf{t}_K^{\lambda}|^2 \delta(E^{\lambda} - \hbar\omega), \quad (11)$$

where  $\Omega$  is the volume of the unit cell, and  $N_k$  is the number of  $k$  points. For left- (+) and right-handed (−) circularly polarized light, polarization vector  $\hat{\epsilon}$  can be defined as  $\hat{\epsilon}_{\pm} = (\hat{x} \pm i\hat{y})/\sqrt{2}$ . Here,  $\mathbf{t}_K^{\lambda}$  is the sum of the electron-hole transition at the  $K$  valley, which can be written as

$$\mathbf{t}_K^{\lambda} = \sum_{v,c} \sum_K^{P_K} A_{vcK}^{\lambda} \frac{\langle \psi_{vK} | \hat{\mathbf{p}} | \psi_{cK} \rangle}{\epsilon_{cK} - \epsilon_{vK}}, \quad (12)$$

where  $\psi_{vK}(\epsilon_{vK})$  are the single-particle Bloch orbitals (energies),  $P_K$  is the region enclosing the  $K$  valley in reciprocal space, and  $\hat{\mathbf{p}}$  is the momentum operator.  $E^{\lambda}$  and  $A_{vcK}^{\lambda}$  are the eigenvalues and eigenvectors of the BSE two-particle Hamiltonian defined in analogy with Ref. [39]. The optical absorption spectrum at the  $K'$  valley,  $\epsilon_{2,K'}$ , can be obtained by replacing  $K$  to  $K'$  in the above equation. As is shown in Figs. 4 and 5(a), 1L TiTeI exhibits pronounced valley-selective circular dichroism. When the magnetic moment is parallel to the  $+Z$  axis, left-handed circularly polarized light can pump valley excitons at the  $K$  valley, while right-handed circular light can generate valley excitons at the  $K'$  valley. Our simulations thus predict that 100% valley polarization

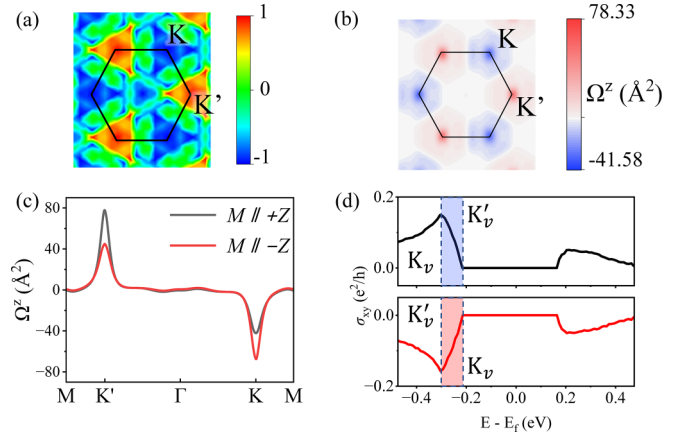


FIG. 5. The anomalous valley Hall effect of 1L TiTeI. (a) The right-handed light conductivity and (b) the total Berry curvature at the first Brillouin zone. The spin polarization is parallel to the  $+Z$  axis. (c) The Berry curvature and (d) corresponding anomalous valley Hall effect at magnetic moment parallel to  $+Z$  and  $-Z$ .

can be achieved upon absorption of circularly polarized light, although electron-phonon scattering (not accounted for in our simulations) is likely to restrict the maximum valley polarization owing to finite temperature effects [41].

Additionally, the optical band gaps between the  $K'$  and  $K$  valleys are not equal. In order to analyze the optical absorption, we have marked the absorption peaks at the  $K'/K$  valleys as A and B excitons, respectively. Exciton A exists in the  $K'$  valley and is excited by right-handed circularly polarized light, while exciton B, excited by left-handed light, exists in the  $K$  valley. As shown in Fig. 3(c), due to the electronic-structure-like valley peak at  $K$  and  $K'$ , the electrons on the valence band will be excited from the valley peak ( $K'/K$ ) to the valley peak of the conduction band ( $K'/K$ ). The excitation energy of excitons A and B is related to the electronic band gap of  $K'/K$  valleys. The energy difference between excitons A and B is 0.08 eV, which is equal to the valley splitting.

The optical selection rule in TiTeI is illustrated in Fig. 1. In the case of a nonmagnetic material, the valley pseudospin leads to a degenerate integrable representation (IR) A into  $1E$  (spin up) and  $2E$  (spin down). The valence band of IR at the  $K$  valley splits to  $1E_{1/2}$  and  $2E_{1/2}$ , while the conduction band of IR splits to  $1E_{3/2}$  and  $2E_{5/2}$ . Conversely, at the  $K'$  valley, the conduction band consists of  $2E_{3/2}$  and  $1E_{5/2}$ . In accordance with the orthogonality theorem, an electric-dipole transition is only allowed if the reduced direct product representation between the initial state IRs and the incident light IRs contains the representation of the final state. When the left-handed light is incident with  $2E$  symmetry, the band on the  $K$  valley meets the excitation condition of  $1E_{1/2} \otimes 2E = 1E_{3/2}$ , allowing for absorption of the left-handed light. On the other hand, the right-handed light can be absorbed at the  $K'$  valley by meeting the excitation condition of  $1E_{1/2} \otimes 1E' = 1E_{5/2}$ . This valley-sensitive circular dichroism demonstrates that 1L TiTeI is an intrinsic ferrovalley material with a chirality-dependent optical band gap.

### E. Anomalous valley Hall effect

Valley polarization in ferrovalley materials is a key factor in the occurrence of various spin-related phenomena, including the valley Hall effect (VHE) and the anomalous valley Hall effect (AVHE). The valley polarization results in the spatial separation of valley excitons with opposite spin, leading to the emergence of a pure spin current [41]. To characterize the AVHE, we calculated the anomalous Hall conductivity ( $\sigma_{xy}$ ) through Wannier functions [25,27,29]. For a 2D ferromagnetic system, the Berry curvature of the  $n$ th band can be written as

$$\Omega_n^z(\mathbf{k}) = - \sum_{n \neq n'} \frac{2\text{Im}\langle \psi_{n\mathbf{k}} | v_x | \psi_{n'\mathbf{k}} \rangle \langle \psi_{n'\mathbf{k}} | v_y | \psi_{n\mathbf{k}} \rangle}{(E_{n'} - E_n)^2}, \quad (13)$$

where the energy level is  $E_n = \hbar\omega_n$ , and  $v$  are the velocity operators. The total Berry curvature derived from the Kubo formula is the sum of all occupied states [27],

$$\Omega^z(\mathbf{k}) = \sum_n f_{nk} \Omega_n^z(\mathbf{k}). \quad (14)$$

The intrinsic  $\sigma_{xy}$  is evaluated by integrating the Berry curvature over the Brillouin zone (BZ),

$$\sigma_{xy} = -\frac{e^2}{\hbar} \int_{\text{BZ}} \frac{d^d k}{(2\pi)^d} \Omega^z(\mathbf{k}), \quad (15)$$

where  $f_{nk}$  is the Fermi-Dirac distribution.

For MoS<sub>2</sub> and WSe<sub>2</sub>, the Berry curvatures are equal in magnitude and opposite in sign at high-symmetry points  $K$  and  $K'$ . If the time-reversal symmetry is broken, the total Berry curvatures are different in magnitude. Figures 5(b) and 5(c) show the Berry curvatures of 1L TiTeI at the first Brillouin zone. Obviously, there are two extreme values at  $K$  and  $K'$ . At other areas in the Brillouin zone, the Berry curvature is almost zero. At the same time, we find that whether the spin polarization is along  $-Z$  or  $+Z$ , their signs at  $K$  and  $K'$  are locked. The nonzero Berry curvature is equivalent to the effect of the magnetic field in reciprocal ( $k$ ) space, causing carriers of opposite spins to accumulate at opposite sides, thus leading to the anomalous Hall effect. Upon applying an in-plane electric field  $E$ , the holes in the valley acquire an anomalous velocity, which is perpendicular to the plane formed by the electric field and the  $Z$  axis,  $\bar{v} \sim \vec{E} \times \vec{\Omega}(k)$ . In addition, the AVHE has been calculated with the WANNIER90 package, shown in Fig. 5(d). When the magnetic moment switches to  $+Z$  ( $-Z$ ), the AVHE appears at the  $K'$  ( $K$ ) valley. The spin-polarized holes will accumulate at the opposite side, which is consistent with the result of Berry curvatures. Consequently, the AVHE device can detect the pure valley Hall current in TiTeI film for storage, computation, and transmission.

### F. Lattice strain induced by substrate

In 2D electronic devices, the lattice mismatch between the substrate and the 2D material can result in an in-plane strain, which has the potential to alter the electrical and magnetic properties of the device. To examine the stability of the ferrovalley feature in the presence of substrate effects, a biaxial in-plane strain was applied to 1L TiTeI. The biaxial strain, represented by  $\varepsilon = (a - a_0)/a$ , was calculated using the lattice constant of 1L TiTeI both with and without the strain,

where  $a$  and  $a_0$  denote strained and equilibrium lattice constants, respectively. Starting from the two-band  $\mathbf{k} \cdot \mathbf{p}$  model, an additional deformation term  $H_\varepsilon$  resulting from a biaxial strain can be written as

$$H_\varepsilon = \frac{D}{2} \varepsilon \hat{\sigma}_0 \hat{\sigma}_z, \quad (16)$$

where  $D$  is the deformation potential. The band gap at the  $K$  and  $K'$  valleys can be simplified as

$$E_g(K) = \Delta + (\lambda_c - \lambda_v) - (m_c - m_v) + D\varepsilon, \quad (17a)$$

$$E_g(K') = \Delta - (\lambda_c - \lambda_v) - (m_c - m_v) + D\varepsilon. \quad (17b)$$

It can be seen that the valley gap can be modulated by a biaxial strain  $\varepsilon$  in a linear fashion, whereby an increase or decrease in strain results in a proportional change in the size of the valley gap. However, the valley splitting, equal to  $2(\lambda_c - \lambda_v)$ , remains constant regardless of the size of the strain. This means that even though the valley gap can be modulated by a strain, the overall energy difference between the valleys remains the same. The fitting parameters of the two-band  $\mathbf{k} \cdot \mathbf{p}$  model have been summarized in Fig. S5 and Table S1 in the Supplemental Material [38]. Here we simulate valley polarization in the range of  $-3\%$  to  $3\%$  substrate strain, shown in Fig. 6(a). Negative and positive signs represent compression and tensile strain, respectively. It is found that the ferrovalley feature in TiTeI remains robust under nonzero strain. The magnitude of valley splitting is closely correlated with the band gap at the  $K/K'$  point.

In addition, the results of Berry curvature at the  $K$  point are presented in Fig. 6(b). The absolute value of Berry curvature increases progressively with increasing biaxial strain. As expressed in the formula, Berry curvature is inversely proportional to the square of the band gap  $[(E_{n'} - E_n)^2]$ . With the increase in strain, the band gap of the TiTeI decreases, resulting in an increase of the Berry curvature. The MAE of TiTeI has been calculated and is displayed in Fig. 6(c). The magnetic moment remains in-plane in the range of  $-3\%$  to  $3\%$  strain. Hence, the magnetic and ferrovalley properties of 1L TiTeI are robust against strain engineering. This means that the substrate selection for the TiTeI material is relatively flexible and the strain induced by the substrate has little effect on the valley polarization and AVHE. Therefore, we believe that 1L TiTeI is an excellent monolayer material for exploring valley polarization and AVHE. Based on the above results, we construct valley-based field-effect transistors in Fig. 6(d). When a horizontal electric field is applied between the left and right electrodes, spin-polarized holes will move to both ends in TiTeI, and accumulate in the vertical direction through AVHE, which can be detected at the top and bottom electrodes. The valley-based field-effect transistors show promise as low-power alternatives to traditional field-effect transistors.

## IV. CONCLUSION

In summary, our work has established the effectiveness of the Janus approach in inducing intrinsic ferromagnetism in nonmagnetic TiI<sub>2</sub>. Compared to TiI<sub>2</sub>, the observed valley splitting of 83 meV in TiTeI is attributed to the combined effects of exchange interaction and spin-orbit coupling. The valence band maximum is contributed by Ti- $d_{x^2-y^2}$  and  $d_{xy}$

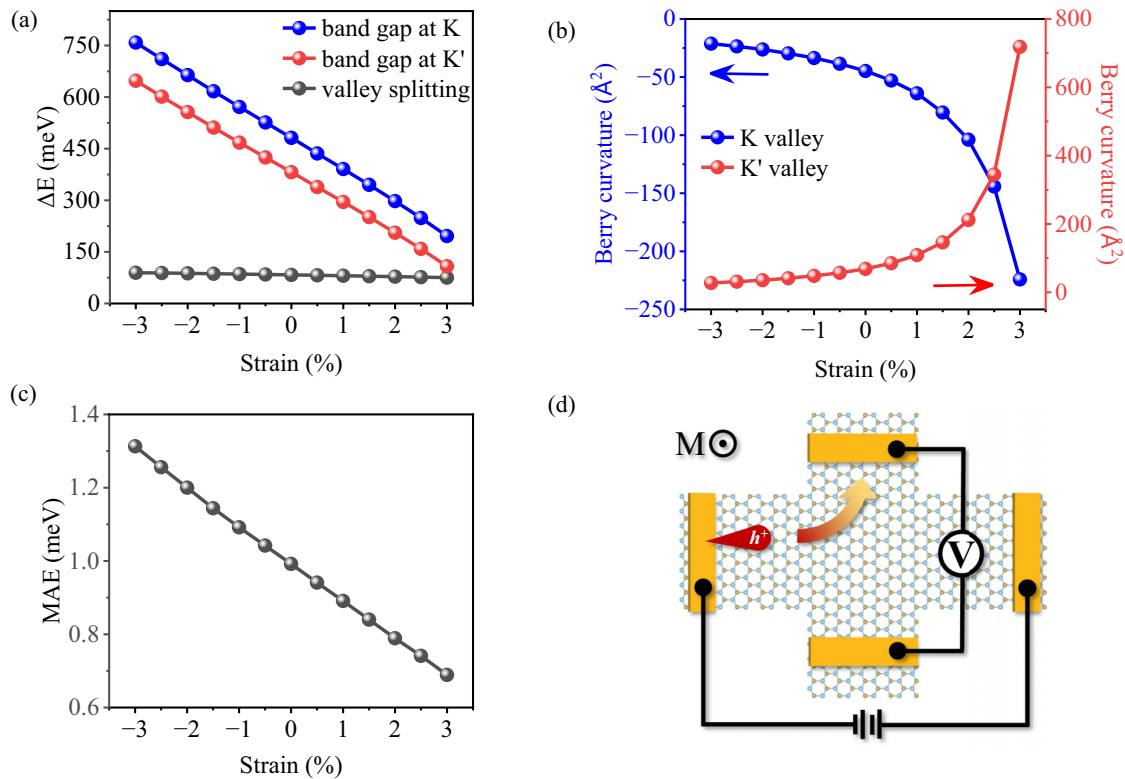


FIG. 6. The valley and magnetic properties of 1L TiTeI. (a) The strain influence of the band gap at the  $K$  (blue) and  $K'$  (red) valleys, and valley splitting between the two valleys (black). (b) The Berry curvature and (c) magnetic anisotropy with a biaxial strain. (d) The anomalous valley Hall device.

orbitals, which are responsible for the valley splitting. Additionally, our *ab initio* calculations based on the many-body BSE approach revealed that TiTeI exhibits valley-selective circular dichroism, leading to the formation of valley excitons at either the  $K$  or  $K'$  valley, thus making it possible to access the valley degrees of freedom by means of circularly polarized light. The occurrence of an anomalous valley Hall effect (AVHE) is facilitated by the application of an in-plane electric field, as evidenced by the valley-contrasting Berry curvature. Our results further indicate that the substrate selection for the TiTeI material is highly flexible, with little impact on the chirality-dependent optical band gap and AVHE

resulting from substrate-induced strain. We believe the Janus method has the potential to greatly impact the field of valleytronics and opens up new avenues for future research and innovation.

#### ACKNOWLEDGMENTS

This work is supported by the National Natural Science Foundation of China (Grant No. 51872145) and the Postgraduate Research & Practice Innovation Program of Jiangsu Province (Grants No. KYCX20\_0748 and No. KYCX19\_0935).

- [1] M. Deng, X. Wang, J. Chen, Z. Li, M. Xue, Z. Zhou, F. Lin, X. Zhu, and Z. Fang, Plasmonic modulation of valleytronic emission in two-dimensional transition metal dichalcogenides, *Adv. Funct. Mater.* **31**, 2010234 (2021).
- [2] A. Kumar, D. Yagodkin, N. Stetzuhn, S. Kovalchuk, A. Melnikov, P. Elliott, S. Sharma, C. Gahl, and K. I. Bolotin, Spin/valley coupled dynamics of electrons and holes at the  $\text{MoS}_2$ - $\text{MoSe}_2$  interface, *Nano Lett.* **21**, 7123 (2021).
- [3] S. Sattar, J. A. Larsson, C. M. Canali, S. Roche, and J. H. Garcia, Giant valley-polarized spin splittings in magnetized Janus Pt dichalcogenides, *Phys. Rev. B* **105**, L041402 (2022).
- [4] W. Y. Tong and C. G. Duan, Electrical control of the anomalous valley Hall effect in antiferrovalley bilayers, *npj Quantum Mater.* **2**, 47 (2017).
- [5] W. Y. Tong, S. J. Gong, X. Wan, and C. G. Duan, Concepts of ferrovalley material and anomalous valley Hall effect, *Nat. Commun.* **7**, 13612 (2016).
- [6] T. Zhou, J. Zhang, H. Jiang, I. Žutić, and Z. Yang, Giant spin-valley polarization and multiple Hall effect in functionalized bismuth monolayers, *npj Quantum Mater.* **3**, 39 (2018).
- [7] X. Liu, A. P. Pyatakov, and W. Ren, Magnetoelectric Coupling in Multiferroic Bilayer  $\text{VS}_2$ , *Phys. Rev. Lett.* **125**, 247601 (2020).
- [8] Y. Liu, Y. Gao, S. Zhang, J. He, J. Yu, and Z. Liu, Valleytronics in transition metal dichalcogenides materials, *Nano Res.* **12**, 2695 (2019).
- [9] Y. Wang, W. Wei, H. Wang, N. Mao, F. Li, B. Huang, and Y. Dai, Janus  $\text{TiXY}$  Monolayers with Tunable

- Berry Curvature, *J. Phys. Chem. Lett.* **10**, 7426 (2019).
- [10] D. Xiao, G. B. Liu, W. Feng, X. Xu, and W. Yao, Coupled Spin and Valley Physics in Monolayers of MoS<sub>2</sub> and Other Group-VI Dichalcogenides, *Phys. Rev. Lett.* **108**, 196802 (2012).
- [11] Y. C. Cheng, Q. Y. Zhang, and U. Schwingenschlögl, Valley polarization in magnetically doped single-layer transition-metal dichalcogenides, *Phys. Rev. B* **89**, 155429 (2014).
- [12] G.-B. Liu, W.-Y. Shan, Y. Yao, W. Yao, and D. Xiao, Three-band tight-binding model for monolayers of group-VIB transition metal dichalcogenides, *Phys. Rev. B* **88**, 085433 (2013).
- [13] E. A. Peterson, J. B. Haber, and J. B. Neaton, Superexchange-induced valley splitting in two-dimensional transition metal dichalcogenides: A first-principles study for rational design, *Phys. Rev. B* **104**, 205421 (2021).
- [14] J. Qi, X. Li, Q. Niu, and J. Feng, Giant and tunable valley degeneracy splitting in MoTe<sub>2</sub>, *Phys. Rev. B* **92**, 121403(R) (2015).
- [15] A. Y. Lu, H. Zhu, J. Xiao, C. P. Chuu, Y. Han, M. H. Chiu, C. C. Cheng, C. W. Yang, K. H. Wei, Y. Yang, Y. Wang, D. Sokaras, D. Nordlund, P. Yang, D. A. Muller, M. Y. Chou, X. Zhang, and L. J. Li, Janus monolayers of transition metal dichalcogenides, *Nat. Nanotechnol.* **12**, 744 (2017).
- [16] T. Hu, F. Jia, G. Zhao, J. Wu, A. Stroppa, and W. Ren, Intrinsic and anisotropic Rashba spin splitting in Janus transition-metal dichalcogenide monolayers, *Phys. Rev. B* **97**, 235404 (2018).
- [17] P. Jiang, L. Kang, Y.-L. Li, X. Zheng, Z. Zeng, and S. Sanvito, Prediction of the two-dimensional Janus ferrovalley material LaBrI, *Phys. Rev. B* **104**, 035430 (2021).
- [18] R. Li, J. Jiang, W. Mi, and H. Bai, Room temperature spontaneous valley polarization in two-dimensional FeClBr monolayer, *Nanoscale* **13**, 14807 (2021).
- [19] C. B. Luo, X. Y. Peng, J. F. Qu, and J. X. Zhong, Valley degree of freedom in ferromagnetic Janus monolayer H-VSSe and the asymmetry-based tuning of the valleytronic properties, *Phys. Rev. B* **101**, 245416 (2020).
- [20] Y.-F. Zhao, Y.-H. Shen, H. Hu, W.-Y. Tong, and C.-G. Duan, Combined piezoelectricity and ferrovalley properties in Janus monolayer VClBr, *Phys. Rev. B* **103**, 115124 (2021).
- [21] P. E. Blochl, Projector augmented-wave method, *Phys. Rev. B* **50**, 17953 (1994).
- [22] G. Kresse and J. Furthmüller, Efficient iterative schemes for *ab initio* total-energy calculations using a plane-wave basis set, *Phys. Rev. B* **54**, 11169 (1996).
- [23] G. Kresse and D. Joubert, From ultrasoft pseudopotentials to the projector augmented-wave method, *Phys. Rev. B* **59**, 1758 (1999).
- [24] S. Grimme, J. Antony, S. Ehrlich, and H. Krieg, A consistent and accurate *ab initio* parametrization of density functional dispersion correction (DFT-D) for the 94 elements H-Pu, *J. Chem. Phys.* **132**, 154104 (2010).
- [25] T. Jungwirth, Q. Niu, and A. H. MacDonald, Anomalous Hall Effect in Ferromagnetic Semiconductors, *Phys. Rev. Lett.* **88**, 207208 (2002).
- [26] A. A. Mostofi, J. R. Yates, Y. S. Lee, I. Souza, D. Vanderbilt, and N. Marzari, WANNIER90: A tool for obtaining maximally-localised Wannier functions, *Comput. Phys. Commun.* **178**, 685 (2008).
- [27] D. J. Thouless, M. Kohmoto, M. P. Nightingale, and M. denNijs, Quantized Hall Conductance in a Two-Dimensional Periodic Potential, *Phys. Rev. Lett.* **49**, 405 (1982).
- [28] X. Wang, J. R. Yates, I. Souza, and D. Vanderbilt, *Ab initio* calculation of the anomalous Hall conductivity by Wannier interpolation, *Phys. Rev. B* **74**, 195118 (2006).
- [29] Y. Yao, L. Kleinman, A. H. MacDonald, J. Sinova, T. Jungwirth, D. S. Wang, E. Wang, and Q. Niu, First Principles Calculation of Anomalous Hall Conductivity in Ferromagnetic bcc Fe, *Phys. Rev. Lett.* **92**, 037204 (2004).
- [30] C. Vorwerk, C. Cocchi, and C. Draxl, Addressing electron-hole correlation in core excitations of solids: An all-electron many-body approach from first principles, *Phys. Rev. B* **95**, 155121 (2017).
- [31] S. Sagmeister and C. Ambrosch-Draxl, Time-dependent density functional theory versus Bethe-Salpeter equation: An all-electron study, *Phys. Chem. Chem. Phys.* **11**, 4451 (2009).
- [32] C. Vorwerk, B. Aurich, C. Cocchi, and C. Draxl, Bethe-Salpeter equation for absorption and scattering spectroscopy: Implementation in the exciting code, *Electron. Struct.* **1**, 037001 (2019).
- [33] A. Gulans, S. Kontur, C. Meisenbichler, D. Nabok, P. Pavone, S. Rigamonti, S. Sagmeister, U. Werner, and C. Draxl, EXCITING: A full-potential all-electron package implementing density-functional theory and many-body perturbation theory, *J. Phys.: Condens. Matter* **26**, 363202 (2014).
- [34] S. Zhang, Y. Wang, S. Wang, B. Huang, Y. Dai, and W. Wei, Electronic properties of monolayer and van der Waals bilayer of Janus TiClI, *J. Phys. Chem. Lett.* **12**, 2245 (2021).
- [35] X. Zhao, F. Liu, J. Ren, and F. Qu, Valleytronic and magneto-optical properties of Janus and conventional TiBrI/CrI<sub>3</sub> and TiX<sub>2</sub>/CrI<sub>3</sub> (X = Br, I) heterostructures, *Phys. Rev. B* **104**, 085119 (2021).
- [36] P. Wang, Y.-X. Zong, H.-Y. Wen, J.-B. Xia, and Z.-M. Wei, Electronic properties of two-dimensional Janus atomic crystal, *Acta Phys. Sin.* **70**, 026801 (2021).
- [37] Y. Guo, J. Dai, J. Zhao, C. Wu, D. Li, L. Zhang, W. Ning, M. Tian, X. C. Zeng, and Y. Xie, Large Negative Magnetoresistance Induced by Anionic Solid Solutions in Two-Dimensional Spin-Frustrated Transition Metal Chalcogenides, *Phys. Rev. Lett.* **113**, 157202 (2014).
- [38] See Supplemental Material at <http://link.aps.org/supplemental/10.1103/PhysRevB.107.174434> for the calculation details of  $N(E_F)$  and  $\Delta_{ex}$ ; the Curie temperature of 1L TiTeI; the band structure of 1L TiI<sub>2</sub> and TiTe<sub>2</sub>; the valley splitting and MAE vs magnetic moment; and the parameters of the two-band  $\mathbf{k} \cdot \mathbf{p}$  model.
- [39] F. Caruso, M. Schebek, Y. Pan, C. Vona, and C. Draxl, Chirality of valley excitons in monolayer transition-metal dichalcogenides, *J. Phys. Chem. Lett.* **13**, 5894 (2022).
- [40] M. Röhlfing and S. G. Louie, Electron-hole excitations and optical spectra from first principles, *Phys. Rev. B* **62**, 4927 (2000).
- [41] Z. Lin, Y. Liu, Z. Wang, S. Xu, S. Chen, W. Duan, and B. Monserrat, Phonon-Limited Valley Polarization in Transition-Metal Dichalcogenides, *Phys. Rev. Lett.* **129**, 027401 (2022).